6

Super-Resolution Procedures in Image and Video Sequences based on Wavelet Atomic Functions

Volodymyr Ponomaryov and Francisco Gomeztagle
National Polytechnic Institute of Mexico
Mexico, Mexico-city

1. Introduction

The images and video sequences obtained from optical, radar, medical sensors, in digital photographs, high definition television, electron microscopy, etc. are formed in the electronic devices, which use different sensors, like x-ray systems, remote sensing cameras, radars, radiometers, US sensors, CCD, etc. (Bovik et al.; 2000, Chaudhuri, 2001; Chaudhuri & Manjunath 2005). So, the images and frames in the video sequences depend on spatial resolution that is defined as a number of pixels per square area in the camera (sensor). The temporal resolution is determined by the frame rate and the exposure time, which limits the maximum speed that can be observed correctly in video. Because of the physical limitations and high cost needed to improve the precision and stability of the imaging system by manufacturing techniques, many applications of image and video sequence data (Farsiu et al., 2004), such as those mentioned above, demand to develop additional methods and algorithms that should restore the resolution degraded in a sensor permitting better observations of the fine details, edges, and restoration of the colour properties. Super-resolution (SR) is defined as a reconstruction of a high-resolution (HR) image or frame in the video sequence from one or multiple low-resolution (LR) images/videos, which is relatively inexpensive to implement. Such methods are effective in the enhancement of the resolution by transcending the limitations of the sensors through digital image processing algorithms. Thus, SR restoration technology is a hot research topic in computer vision applications (Park et al., 2003, Zhang et al., 2010).

This chapter is devoted to analysis of the various ways and methods to get SR in the images or video sequences (Protter et al., 2009; Park et al., 2003). So, it is assumed that the images or frames are treated as LR ones, where the promising methods of super resolution to the entire image or area of interest should be employed recovering the data lost during acquisition stage. Finally, reconstructed data present more information for better visual understanding of selected areas, permitting a deeper analysis for various purposes (Baboulaz et al., 2009)

There are exist a lot of the algorithms in the SR (Franzen et al., 2001; Chaudhuri et al., 2001), among them, the nearest neighbour methods that employ the interpolation procedure with the closest pixels to approximating point; bi-linear interpolation (Hou et al., 1978) that

applies the mean averaging filter for neighbouring pixels in each a central pixel, and in this way obtaining the lost pixels; the bi-cubic algorithm that uses the cubic polynomial function for additional pixels; the methods based on spline technique (Lehmann et al., 1999; Phu et al., 2004) that deform the edges and wave them. Simple interpolation-based methods, such as bilinear or bicubic interpolation, etc. tend to produce HR images with jagged edges, these are a common artifacts for many SR algorithms. All these methods only apply the spatial pixels information. Other algorithms are known in literature, among them, warping, which is based on re-sampled operation on base on rectangular point spread function, and methods based on fuzzy logic theory (Tolpekin et al., 2008). Another group of methods is based on the Fourier transform with band limited function interpolation. Here, the restoration is realized by extension of the zeros, applying Discrete Fourier transform (DFT) (Crouse et al., 1998; Maeland et al., 1998; Landi et al., 2006) of size N for original sequence, filling up it with the zeros from N + 1 to 2N, and finally, calculating 2N points in the inverse DFT, that permits improving the detail and edge preservation in SR image. In similar way, this idea can be used employing the Discrete Cosine Transform (DCT) to find the lost pixels in an image or video frame, reconstructing SR image via inverse transform as in DFT method. The Wavelet based techniques have been introduced but mainly in specific applications (Crouse et al., 1998; Maeland et al., 1998; Landi et al., 2006, Reichenbach et al., 2003.; Chan et al., 2003; Lertrattanapanich et al., 2002; Ng et al., 2004).

The proposed here techniques take into account the spatial and spectral Wavelet pixel information permitting to reconstruct different video (Katsaggelos et al., 2007; Chaudhuri&Manjunath, 2005; Qin Feng-qing et al.; 2009, C. Wang et al, 2006) composition and texture nature, and, as it is observed from realized simulations, present good performance in terms of objective and subjective criteria (Chan et al., 2003; Lertrattanapanich et al., 2002; Ng et al., 2004).

Here, we describe in details the novel SR method applying the Wavelets based on atomic functions (WAF) (Gulyaev et al., 2007). Novel Wavelet families (*Fup, Up, Gk, Ξn, π*) that are employed in SR restoration present the better performance in the compression of different types of the images and video sequences due to its special approximation properties explaining in this chapter. Recently, WAFs have already demonstrated their successful performance in the diverse fields, such as windowing in radar processing, compression and recognition of medical images, speech reconstruction, image processing, etc. (Juarez et al.; 2008, Kravchenko et al.; 2008, Kravchenko et al., 2009). So, it is also expected better estimation of lost information and possible improvement during reconstruction in the SR procedure. Additionally, the most common Wavelet families, such as Daubechies, Symlets, Biorthogonal and Coiflets are tested also.

The idea applied in Wavelet based techniques is justified by such a proposition: If Wavelet transform is efficiently used in the compression and decompression of the images without significant lost of information, then it is supposed that the reconstruction of HR image or frame in a video sequence can be realized sufficiently well using the inverse Wavelet transform, so treating the initial LR image as a before compressed one. In such a way, the reconstruction of SR data is realized by extension of an image (frame) size up to 4 times in comparison with the original LR image.

Due to movement of an object or a scene during the video acquisition process, the frames are different from each other, so, utilizing the spatial sub pixel movement information between the frames, a spatial HR video sequence can be reconstructed from a LR video

(Shen Huanfeng et al.; 2007, Callico et al., 2008). Principally, this permits to restore the high frequencies behind the diffraction limit of a sensor. For neighbouring frames in the video sequences, which can be significantly different because of motion, the similar pixels are tested with the purpose to find the movement estimate (Jain et al., 1981). Such motion estimation is used to obtain the better estimates of the missing values. The apparent motion vectors are calculated between two neighbouring frames obtaining additional pixels. The precision of the registration stage is an important for the reconstructed image quality, because sometimes it is better to interpolate a LR image using classical algorithms than to reconstruct a HR image/frame from a set of images applying incorrect motion parameters.
In the chapter, the proposed methods are also investigated under criterion of real time implementation, where additionally to restoration quality, the time values needed to reconstruct is considered, so, only fast method in motion estimation and SR are employed here, like "block matching" that commonly is used (Gomeztagle et al., 2009).
To compare the robustness of the analyzed methods different test images and video sequences are studied, These image data present various physical characteristics, such as fine details, edges, texture, contrasts, smooth and rough background, etc. Test video sequences: "Toy", "Plant", "Walter", "Stephan" and "Flowers" have been investigated in greyscale and colour formats.
To get objective performance of reconstruction, the criteria: Pick Signal to Noise Ratio (PSNR), Mean Absolute Error (MAE), and Normalized Colour Difference (NCD) are employed (Bovik, 2000; Kravchenko et al.; 2009; Farsiu et al., 2006; Akgun et al., 2005; Wood et al., 2008).
Finally, the possibility of the real time processing is discussed implementing several promising frameworks on the Texas instruments Digital Signal Processing (TMS320C642, 2004).

2. Performance Criteria

There exist different objective measures that are used in evaluation of image restoration qualities. Here, to characterize different known and proposed SR algorithms, and compare their performances, several criteria are employed: the Peak Signal-to-Noise Ratio (*PSNR*) for the characterization of noise suppression and artifacts limitations, Mean Absolute Error (*MAE*) for quantization of edges and fine detail preservation, and the Normalized Color Difference (*NCD*) for the estimation of the color perceptual error (Bovik, 2000; Kravchenko et al., 2009) The PSNR is defined as:

$$PSNR = 10\log\left(\frac{(255)^2}{MSE}\right), \text{ dB}, \tag{1}$$

where the Mean Square Error (*MSE*) is the error measure for gray scale image of dimension MN (Bovik, 2000).
The *MAE* criterion is written as follows:

$$MAE = \frac{1}{M \times N}\sum_{x=0}^{M-1}\sum_{y=0}^{N-1}\left|\left[\hat{f}(x,y) - f(x,y)\right]\right| \tag{2}$$

Every measure, *PSNR* and *MAE* to get the objective criteria value employ the reference image HR $f(x,y)$ and other one $\hat{f}(x,y)$ obtained from SR algorithm.

NCD criterion should be calculated in the $L^*u^*v^*$ space (Katsaggelos et al., 2007; Kravchenko et al., 2009)) and is a measure of color errors:

$$\mathrm{NCD} = \frac{\sum_{i=1}^{M_1}\sum_{j=1}^{M_2}\left\|\Delta f_{Luv}(i,j)\right\|_{L_2}}{\sum_{i=1}^{M_1}\sum_{j=1}^{M_2}\left\|f^*_{Luv}(i,j)\right\|_{L_2}} \tag{3}$$

Here, $\left\|\Delta f_{Luv}(i,j)\right\|_{L_2} = \left[\left(\Delta L^*(i,j)\right)^2 + \left(\Delta u^*\right)^2 + \left(\Delta v^*\right)^2\right]^{1/2}$ is the norm of color error; ΔL^*, Δu^*, and Δv^* are the differences in the L^*, u^*, and v^* components, respectively, between the two color vectors that present the SR reconstructed image and original HR image for each a pixel *(i, j)* of an image; and $\left\|f^*_{Luv}(i,j)\right\|_{L_2} = \left[\left(L^*\right)^2 + \left(u^*\right)^2 + \left(v^*\right)^2\right]^{1/2}$ is the L_2 norm or magnitude of the original HR image pixel vector in the $L^*u^*v^*$ space. It has been proved that the *NCD* objective measure expresses well the color distortion (Kravchenko et al., 2009).

Since it is difficult to define the error criteria for an accurate quantization of SR image reconstruction, a subjective measure of the image distortion in form of subjective visual perception is used in this paper. It is presented by error image - the absolute difference between the original HR image and reconstructed SR one. So, subjective visual comparison of the images provides information about the spatial distortion and artifacts introduced by an algorithm employed, and present the performance of the analyzed technique when the SR image or SR frame of the video sequence are observed by the human visual system.

The motion estimation is one of the fundamental problems in the treatment of the digital video sequences (Wüst Zibetti et al. 2007; Callico et al., 2008; Kravchenko et al., 2009). The objective of motion estimation consists of calculating the field of motion vectors to describe the apparent movement between two images of the sequence. It is important to deal with apparent movement, because the dynamic changes (motions) of the images are the projection on 2D plane at discrete moments of time from 3D spatial-temporal scenes. This supposes a loss of information that does necessary to distinguish between the real movement that projects on the plane and the movement pretends that, well, to keep redundant information with the goal to improve the estimate. In this specific application, the estimations of the movements between the frames should be found, and the technique "block matching" is usually used (Callico et al., 2008). Because this technique is too expensive in computation charge, we apply the motion estimation only in areas where two images have differences. A set of pixels in a window of sizes 9 x 9 pixels in a first frame, that should be slipped into the next frame is used in order to find the minimum of the difference

according to criterion: $E(d) = \sum_{x \in R} \left| f_t(x) - \hat{f}_{t,\tau}(x + d(x)) \right|$. In such a way, it is possible to obtain the redundant information from two blocks. So, we can use the information in the same zone of a scene that is found in two frames, in order to increase the sample size permitting the correct estimation of the lost pixels. The mentioned above algorithm in motion estimation permits to form the lost pixels in the SR reconstruction, and it is simple and sufficiently fast. There exist a lot of other algorithms with better performance but their computational charges are sufficiently bigger, this does not provide their real time implementation.

3. Wavelet Atomic Functions and their Properties

3.1 Atomic Functions

Let present novel family of the Wavelets, the WAF, firstly introducing basic atomic functions (*up*, fup_n, g_k, up_n, Ξ_n, π_n) used as mother functions in their Wavelets construction. The idea of AF was consisted of finding a function where the maximum and minimum of their derivatives should be similar to maximum of initial function. The result of such a mathematical problem is in infinitely differentiable solution of the differential equations with a shifted argument (Kravchenko et al., 2008, 2009; Gulyaev et al., 2007):

$Lf = \lambda \sum_{k=1}^{n} c(k) f[ax - b(k)]$, $|a| > 1$, where L is a linear differential operator with constant coefficients. It has been shown that AFs take intermediate "place" between splines and classical polynomials. Similarly to *B*-splines AFs are compactly supported and similarly to polynomials they are universal from the point of view of their approximation properties. AFs are useful in numerical analysis, in the cases when an approximated function is smooth enough and the use of polynomials is inconvenient due to the fact that they are not compactly supported.

The simplest and most important AF is generated by infinite-to-one convolutions of rectangular impulses. To investigate such a convolution we use the Fourier transform. Applying standard Fourier transform, the rectangular impulse is represented as: $\varphi(x) = \frac{1}{2\pi} \int_{-\infty}^{\infty} e^{jux} \frac{\sin(u/2)}{u/2} du$; analogously, the *N-to-one* convolution of *(N+1)* identical rectangle impulses $\varphi(x)$ defines the compactly supported spline $\theta_N(x)$:

$$\theta_N(x) = \frac{1}{2\pi} \int_{-\infty}^{\infty} e^{jux} \left(\frac{\sin(u/2)}{u/2} \right)^{N+1} du . \tag{4}$$

The function *up(x)* is represented by Fourier transform for the infinite convolution of rectangular impulses with variable length of duration 2^{n-1} similar to eq. (1)

$$up(x) = \frac{1}{2\pi} \int_{-\infty}^{\infty} e^{jux} \prod_{k=1}^{\infty} \frac{\sin(u \cdot 2^{-k})}{u \cdot 2^{-k}} du \tag{5}$$

The Atomic Functions $fup_N(x)$ is defined by the convolution of compactly supported spline $\theta_N(x)$ and AF $up(x)$ in the interval $\left[-(N+2)/2,(N+2)/2\right]$:

$$fup_N(x)=\theta_N(x)*up(2x)=\theta_{N-1}(x)*up(x),\quad fup_0(x)\equiv up(x). \tag{6}$$

The Fourier transform of $fup_N(x)$ is written as follows:

$$fup_N(x)=\int_{-\infty}^{\infty}e^{jux}\left(\frac{\sin(u/2)}{u/2}\right)^N\prod_{k=1}^{\infty}\frac{\sin\left(u\cdot 2^{-k}\right)}{u\cdot 2^{-k}}du\,, \tag{7}$$

Next AF $\Xi_n(x)$, which is used here, is defined as a compactly supported solution of the equation:

$$y^n(x)=a\sum_{k=0}^{n}C_n^k(-1)^k\,y\left[(n+1)x+n-2k\right],\quad x\in\left[-1,\ \ 1\right]. \tag{8}$$

Using transforms analogous to those made in (Kravchenko et al., 2009), we obtain the following integral representation for AF $\Xi_n(x)$:

$$\Xi_n(x)=\frac{1}{2\pi}\int_{-\infty}^{\infty}\exp\{ixt\}\prod_{k=1}^{\infty}\left(\frac{\sin t(n+1)^{-k}}{t(n+1)^{-k}}\right)^n dt\quad,\ \Xi_1(x)=up(x). \tag{9}$$

Another AF $g_k(x)$ employed in this work is defined in (Kravchenko et al., 2009), as the compactly supported solution of differential equation in form of the Fourier transforms:

$$g_k(x)=\frac{1}{2\pi}\int_{-\infty}^{\infty}F_k(t)\exp\{-itx\}dt, \tag{10}$$

Where $F_k(t)=\prod_{j=1}^{\infty}\frac{k^2}{1-2\cos(2k/3)}\frac{\left[\cos\left(2t3^{-j}\right)-\cos(2t/3)\right]}{k^2-t^2 9^{1-j}}$; $a=\frac{2}{3}\frac{k^2}{1-\cos(2k/3)},b=2a\cos(2k/3)$.

Next AF $\pi_m(x)$ considers the differential equation:

$\pi'_m(x)=a\left[\pi_m(x_1(m))+\sum_{k=2}^{2m-1}(-1)\pi_m(x_k(m))-\pi_m(x_{2m}(m))\right]$, where $x_k(m)=2mx+2m-2k+1, x\in R^1$, $k=\overline{1,2m};\ m=3,4,...,$, and can be presented using the Fourier transform:

$$F_m(t)=\prod_{k=1}^{m}\frac{\left[\frac{\sin(2m-1)t}{(2m)^k}+\sum_{v=2}^{m}(-1)^v\frac{\sin(2m-2v+1)t}{(2m)^k}\right]}{(3m-2)t/(2m)^k} \tag{11}$$

Finally, the AF $up_m(x)$ used below is the generalization of presented above AF $up(x)$, and can be characterized by their Fourier transform (Kravchenko et al., 2009)**:**

$$up_m(x)=\frac{1}{2\pi}\int_{-\infty}^{\infty}e^{jxu}\prod_{k=1}^{\infty}\frac{\sin^2\left(\frac{mu}{(2m)^k}\right)}{\frac{mu}{(2m)^k}m\sin\left(\frac{u}{(2m)^k}\right)}du \quad , m=1, 2, 3, \quad up_1(x)=up(x) \tag{12}$$

Let explain the construction procedure for WAFs and their properties (Gulyev et al., 2007). Each a WAF with unit norm has such a structure:

$$\psi_\theta^p(x)=\frac{\exp(j\pi x)h_\theta^p(x)}{\left\|h_\theta^p(x)\right\|}. \tag{13}$$

The function $h_\theta^p(x)$ in eq. (13) is determined as:

$$h_\theta^p(x)=\frac{1}{2^p}\sum_{k=0}^{(p-1)/2}C_p^k\left(\theta(x+\frac{p-2k}{2})+\theta(x-\frac{p-2k}{2})\right) \quad \text{odd } p, \tag{14a}$$

$$h_\theta^p(x)=\frac{1}{2^p}\left[\sum_{k=0}^{(p-2)/2}C_p^k\left(\theta(x+\frac{p-2k}{2})+\theta(x-\frac{p-2k}{2})\right)+C_p^{p/2}\theta(x)\right] \text{ even p,} \tag{14b}$$

where $\widetilde{\theta}(\omega)$ is the spectrum of chosen atomic function $\theta(x)$ from presented above in eqs. (5), (7), (9) - (12).

3.2 Wavelet Key Properties

Inverse Discrete Wavelet Transform (IDWT) is applied in reconstruction of SR image. The DWT and IDWT are usually implemented employing the filter bank techniques in the scheme with only two filters for rows. The Wavelet decomposition algorithm applies two analysis filters $\widetilde{H}(z)$ (lowpass) and $\widetilde{G}(z)$ (highpass), and the reconstruction algorithm uses the complementary synthesis filters *H(z)* (lowpass) and *G(z)* (highpass). The highpass operators are obtained by simple shift and modulation presented as $\widetilde{G}(z)$ = *z H(-z)* and

$G(z) = z^{-1}\widetilde{H}(-z)$. The WT involves the scaling functions $\varphi(x) = \frac{2}{H(1)}\sum_{k\in Z} h_k \varphi(2x-k)$, where the wavelets themselves are linear combination of the scaling functions: $\psi(x) = \frac{2}{H(1)}\sum_{k} g_k \varphi(2x-k)$. The corresponding analysis and synthesis Wavelet basis functions are $\widetilde{\psi}_{i,k} = 2^{-i/2}\widetilde{\psi}(x/2^i - k)$ and $\psi_{i,k} = 2^{-i/2}\psi(x/2^i - k)$, respectively, where *i* and *k* are the translation and scale indices.

Frequency response allows appreciating the behavior of the synthesis filters (in SR problem) in a graphic way to appreciate the differences of the different Wavelet families used.

Approximation order implies that the scaling function $\varphi(x)$ reproduces all polynomials of degree lesser or equal to $n = L - 1$. The stability of the wavelet representation and its underlying multi-resolution bases are depended on translations the scaling functions and how wavelets form Riesz bases (Meyer, 1990). To analyze this the *Cross-correlation* function is defined as a 2π periodic function $a_{\varphi 1,\varphi 2}(\omega)$: $a_{\varphi 1,\varphi 2}(\omega) = \sum_{k\in Z} e^{-kj\omega}\varphi_{12}(k)$, where $\varphi_{12}(x) = \int \varphi_2(\xi)\varphi_1(\xi + x)d\xi$.

Riesz bounds. The tightest upper and lower bounds, $B < \infty$ and $A > 0$ of the autocorrelation filter are the Riesz bounds of $\varphi(x)$ and given by: $A^2 = \inf_{\omega\in[0,2\pi]} a_\varphi(\omega)$, $B^2 = \sup_{\omega\in[0,2\pi]} a_\varphi(\omega)$, satisfying to the next equations: $A = \inf_{c\in\ell^2} \frac{\left\|\sum_{k\in Z} c_k \varphi(x-k)\right\|_{L^2}}{\|c\|_{\ell^2}}$, and $B = \sup_{c\in\ell^2} \frac{\left\|\sum_{k\in Z} c_k \varphi(x-k)\right\|_{L^2}}{\|c\|_{\ell^2}}$. The existence of the Riesz bounds ensures that the underlying basis functions are in L^2 and that they are linearly independent (in the ℓ^2 space). The Riesz basis property expresses equivalence between the L^2-norm of the expanded functions and the ℓ^2-norm of their coefficients in the wavelet or scaling function basis. There is a perfect norm equivalence (Parseval's relation), if and only if $A = B = 1$, so, in this case the basis is orthonormal.

Projection angle θ between the synthesis and analysis subspaces V_a and $\widetilde{V}_a$ is defined as: $\cos\theta = \inf_{f\in\widetilde{V}_a} \frac{\|\mathrm{P}_a f\|_{L^2}}{\|f\|_{L^2}} = \frac{1}{\sup_{\omega\in[0,2\pi]} \sqrt{a_\varphi(\omega)\cdot a_{\widetilde{\varphi}}(\omega)}}$; this fundamental quantity is scale-independent, and it allows comparing the performance of the biorthogonal projection $\widetilde{\mathrm{P}}_a$ with that of the optimal least squares solution P_a for a given approximation space V_a (Kravchenko et al., 2008): $\forall f \in L^2, \quad \|f - \mathrm{P}_a f\|_{L^2} \le \|f - \widetilde{\mathrm{P}}_a f\|_{L^2} \le \frac{1}{\cos\theta}\|f - \mathrm{P}_a f\|_{L^2}$.

The biorthogonal projector will be essentially as good as the optimal one (orthogonal projector onto the same space) provides that *cos θ* is close to one.

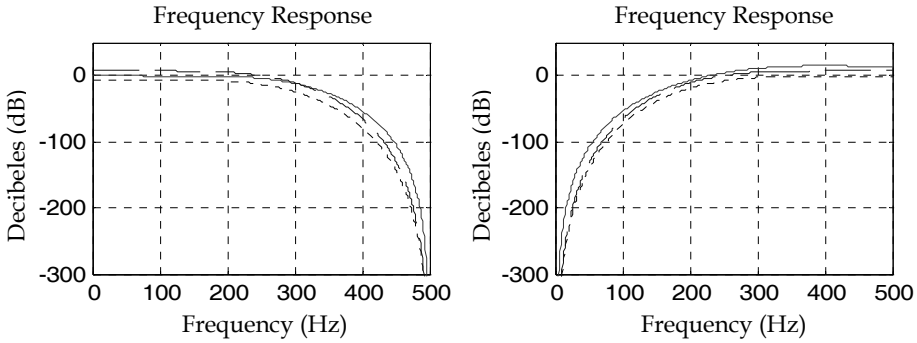

Fig. 1. Frequency responses: Wavelet 9/7 (solid line), Daubechies 8 (dotted line), and Symlet 8 (dashed line).

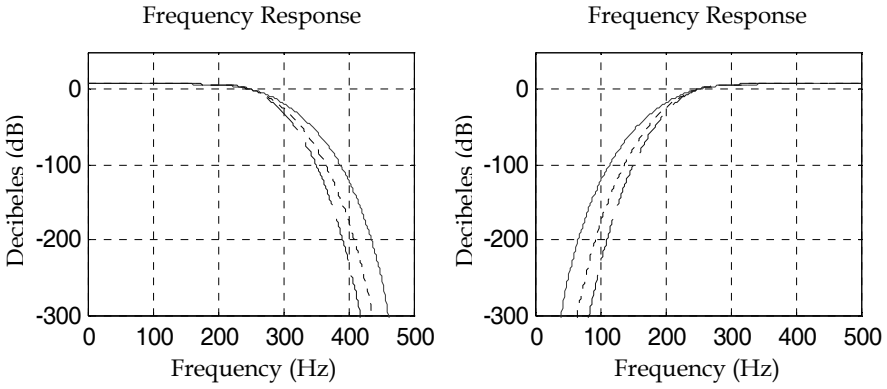

Fig. 2. Frequency responses: WAFs up(*t*) (solid line), $\text{fup}_2(t)$ (dotted line), and eup(*t*) (dashed line).

Figure 1 and 2 expose the frequency responses for some classical Wavelets and WAFs, accordingly, showing that Daubechies and Symlet filters are more selective that the Wavelet 9/7 filters.

It has been observed that the WAF filters have an respond function answer in more selective frequency that the better classical, potentially permitting the best approximation quality in the SR problem.

Finally, Table 1 presents the key properties of the different Wavelets used in SR of the images (Kravchenko et al., 2008). So, the approximation property of estimation is characterized by relative error $\delta = 2(1-r)$, where *r* is correlation coefficient that is equal to projection cosine in this case, the calculations have shown that WAF based on *eup(x)* can potentially produce relative variance error of 0,00464 (6.8% in RMS value), Wavelet *Db8*

gives the value of 0,02242 (of about 15% in RMS value), and *Wavelet 9/7* presents the value of 0,03234 (more than 18% in RMS value). The existence of the limits Riesz bounds demonstrates that the coefficients of the analysis and synthesis filters are lineally independent. The found projection cosine shows that the WAFs are near to the ideal value, this implies that they are better semi-orthogonal and the "most independent". These properties permit to expect that the families of WAFs have sufficiently better acting in approximation problems such as SR one than the traditional families.

Key properties for different Wavelet filters												
Type	**Wavelet 9/7**		**Daubechies 8**		**Symlet 8**		**WAF *up(t)***		**WAF *fup* $_2$*(t)***		**WAF *eup(t)***	
	Dec.	Rec.	Dec.	Rec.	Dec.	Rec.	Dec.	Rec.	Dec.	Rec.	Dec.	Rec.
Approximation Order	4		4		4		4		4		4	
Projection cosine	0.98387		0.98879		0.98781		0.99176		0.99472		0.99769	
Riesz Bounds	0.926	0.943	0.833	0.849	0.880	0.896	0.792	0.806	0.713	0.726	0.641	0.653
	1.065	1.084	1.267	1.290	1.273	1.295	1.514	1.542	1.802	1.834	2.145	2.183

Table 1. Summary of key properties of different Wavelet families.

4. Some Promising Frameworks in Image and Video Super-Resolution

Resolution enhancement via probabilistic deconvolution of multiple degraded images (Sroubek et al. 2006). This approach consists of employing a stochastic fusion method that performs multichannel blind deconvolution (MBD) and SR simultaneously. LR image z_k is modeled by unknown blurring the ideal image $\boldsymbol{u}$, and shifting the result by an unknown vector contaminated by Gaussian noise. This model is a very realistic description of remote sensing observation process where many LR satellite sensors (channels) are employed, and can be rewritten as:

$$z = Gu + n = Ug + n\,, \tag{15}$$

Where $z \equiv \left[z_1^T,\ldots,z_K^T\right]^T, G \equiv \left[zG_1^T,\ldots,G_K^T\right]^T,^T \quad n \equiv \left[n_1^T,\ldots,n_K^T\right]^T, g \equiv \left[g_1^T,\ldots,g_K^T\right]^T$ and $\boldsymbol{U}$ is a block-diagonal matrix with $\boldsymbol{K}$ blocks each performing convolution with an image $\boldsymbol{u}$. According to the Bayes solution, the relation between a priori probabilities $\boldsymbol{p(u)}$, $\boldsymbol{p(g)}$ and the a posteriori probability is $\boldsymbol{p(u,g|z)=const\ p(z|u,g)p(u)p(g)}$, where the conditional pdf $\boldsymbol{p(z|u,g)}$ is follows from Gaussian noise approximation, prior Gibbs pdf for $\boldsymbol{u}$, where the last is defined as

$$p(u)=\begin{cases}\frac{1}{z}\exp\left\{-\frac{1}{2\sigma_u^2}u^T L(v)u\right\} & if\ u\in C_u\\ 0 & otherwise\end{cases},\quad C_u\equiv\left\{u\middle|0\le u\le 255\right\}, \tag{16}$$

and the following prior distribution for g is used:

$$p(g)=\begin{cases}\frac{1}{Z}\exp\left\{-\frac{1}{2}g^T\Im^T D^{-1}\Im g\right\} & if\ g\in C_g\\ 0 & otherwise\end{cases} \tag{17}$$

The optimal MBD solution is defined as a maximum a posteriori (MAP) estimate. It does not require any knowledge of the blurring functions and the input channels might be mutually shifted by an unknown vector. Allowing only translational between-channel the MAP estimation is given as:

$$\{\hat{u},\hat{g}\}=\arg_{u\in C,g\in Cg}\min\left\{(z-Gu)^T\sum{}^{-1}(z-Gu)+\frac{1}{\sigma_u^2}u^T L(v)u+g^T\Im^T D^{-1}\Im g\right\} \tag{18}$$

The genetic algorithms are applied adopting an approach of alternating minimizations over u and g. The proposed AM-MAP algorithm alternates between two steps:

$$1.\ \hat{u}=\left(G^T\Sigma^{-1}G+\frac{1}{\sigma_u^2}L(v)\right)^{-1}G^T\sum{}^{-1}Z\wedge u\in C_u, \tag{19a}$$

$$2.\ \hat{g}=\left(U^T\Sigma^{-1}U+\Im^T D^T\Im\right)^{-1}U^T\sum{}^{-1}z\wedge g\in C_u, \tag{19b}$$

Here, a decimation operator matrix D is introduced to model a LR acquisition of digital sensors by performing convolution with a 2X 2 uniform mask returns every second pixel and down-sampling of images. In the discrete case, the acquisition model becomes $Z=\mathrm{DGu}+\mathrm{n}$. The steps in the AM-MAP algorithm are the same, except the G, U and $\Im$ are replaced with DG, DU and $\Im D$, respectively. An iterative fusion algorithm was developed recovering a HR image from misaligned and blurred input channels. The fusion problem is formulated as the MAP estimation with the prior probabilities derived from the variational integral and from the mutual relation of co-prime channels. The simulation results of an approach expose that framework can form high-quality fused images. Recovering SR and blind deconvolution, the method can restore the images as it shown in Fig.3 The data source for simulation (playing the role of the *ideal* image) was the 300×300 SPOT HRV image covering the north-western part of Prague (Czech capital). LR acquisitions are formed blurring image by randomly generated 6×6 motion masks, corrupted by AWGN of SNR = 50 dB and resolution decimated by factor of two to obtain images of size 150×150. Six such images were generated and used as input channels´ data.

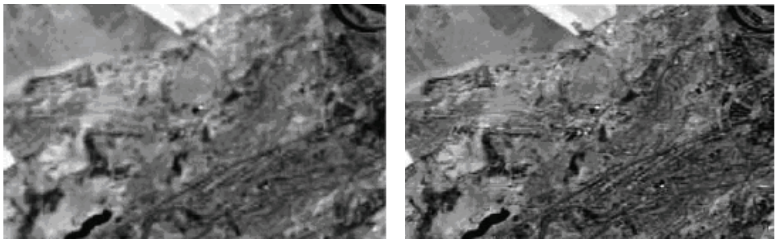

a) b)

Fig. 3. a) Standard MBD fusion, followed by linear interpolation; (b) fusion using AM-MAP with the SR.

The result of fusion using the blind deconvolution approach in (Flusser, 2003) and applying linear interpolation afterward is depicted in Fig. 3(a). The current algorithm with the SR extension performs better and gives a more accurate representation of the original image, as illustrated in Fig. 3(b).

SR Reconstruction Algorithm for Surveillance Images (Zhang et al., 2010) is presented as an edge-preserving maximum a posteriori (MAP) estimation based SR algorithm using a Weighted Directional Markov image prior model for a region of interest (ROI) from several LR surveillance images. In many surveillance video applications, it is of interest to recognize an object that is selected as a ROI where edges of the object are often very important. Standard Gaussian Markov Random Field regularization (GMRF) in the MAP-based SR cannot effectively preserve sharp edges in the estimated images. Different techniques have been proposed such as Huber-Markov regularization and bilateral-TV regularization, Weighted Directional Markov image prior model, which utilizes the weights for different directional smoothness measures of the edge pixels (Chan et al., 2003, Lertrattanapanich et al., 2002). Typically, the imaging process involves warping, followed by blurring and down-sampling to generate LR images from the HR image. So, the LR image can be represented as $y_k = DB\ M_k z + n$, where $\boldsymbol{M}_k$ is warp matrix, $\boldsymbol{B}$ is camera blur matrix, $\boldsymbol{D}$ is down-sampling matrix, and $\boldsymbol{n}$ is noise, k= *1,2,....P*, with P being the number of LR images. It is assumed that the motion of the ROI during the sequence is a globally translational motion and the motions of all points can often be modelled by a parametric model.

In most situations, the problem of SR is an ill-posed inverse one because the information contained in the observed LR images is not sufficient to solve the HR image, so the ill-posed problem should be stabilized to be well-posed. The MAP method, which can easily include image prior or regularization, is an efficient framework to describe the SR problem.

The maximization of this posterior probability distribution is equivalent to such a problem:

$$\hat{z} = \arg \ \min\left[\sum_k \left\| y_k - A_k z \right\|^2 + \lambda \Gamma(z)\right], \tag{20}$$

where the first term is the data fidelity term, and $\Gamma(z)$ is the regularization term.

Here, the CG optimization utilizes conjugate direction instead of local gradient to search for the minima permitting faster convergence when compared to the steepest descent method. The gradient of presented above function is denoted as

$$r\left(\hat{z}^{n}\right)=\sum_{k} A_{K}^{T}\left(A_{k}\hat{z}^{n}-y_{k}\right)+\lambda\nabla\Gamma\left(\hat{z}^{n}\right), \tag{21}$$

where the right term of the gradient $\nabla\Gamma\left(\hat{z}^{n}\right)$ is the derivative of the regularization term with respect to z and can be approximated from the estimated HR image. While the left term $A_k^T\left(A_k\hat{z}^n-y_k\right)=M_k^T B^T D^T\left(DBM_k\hat{z}^n-y_k\right)$ can be computed using basic image operations such as warp, blur and sampling instead of sparse matrices multiplications. The matrices $\boldsymbol{M_k, B, D}$ model the principal image formation process: the image warping, blurring and down-sampling, respectively. The implementation of their transpose matrices is also very simple D^{T} is implemented by up-sampling the image without interpolation, i.e., by zero padding. For a convolution blur, B^{T} is the convolution with the flipped kernel of the imaging blur kernel $b(\mathrm{i},\mathrm{j})$; If M_{k} is implemented by backward warping, then M_K^T should be the forward warping of the inverse motion. Thus, the gradient of the cost function with the Weighted Markov Random Field (WMRF) regularization is computed in an efficient manner and the CG optimization technique is used without explicit construction of these large matrices.

The simulation results presented in following figures show the effectiveness of the current proposal (Fig. 4). The image was reconstructed using MRF and WMRF regularizations, and this scenario can be thought of as a SR reconstruction problem with a resolution enhancement factor of one. For the quadratic function chosen as the function of the smooth measure, the reconstruction result of GMRF regularization is shown in Figure 4(a) and Figure 4(b), and GMRF regularization achieves the smallest MSE error of 18.79 ion comparison with other investigated techniques.

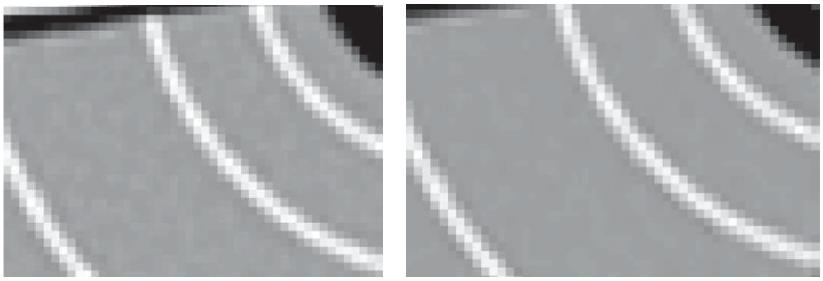

a) b)

Fig. 4. Simulation results of deblurring using different regularizations. (a) HMRF regularization. (b) HWMRF regularization.

Filters	GMRF	GWMRF	HMRF	HWMRF
First experiment	18.79	14.61	12.91	9.73
Second experiment	77.54	72.02	71.85	62.51

Table 2. MSE error of super- resolution reconstruction using different regularizations.

Representation of HR Images from Low Sampled Fourier Data (LandiI et al., 2006). B-spline functions are proposed to use for the parametric representation of HR images from low sampled data in the Fourier domain. To solve the ill-conditioned linear system arising from the method an efficient regularization method is proposed demonstrating this in applications to dynamic Magnetic Resonance images (MRI) that acquires a time series of images of the same slice of a body where the data are low sampled in the Fourier space to fasten the acquisition. The image representation problem from limited Fourier data is classically addressed as an interpolation problem through zero padding in the Fourier domain but this born in substantially degraded HR images truncation artifacts, including ringing and blurring artifacts. In current method, the desired HR image is represented through a B-spline parametric model where the coefficients are determined. In practical applications, the band-limited interpolator based on *sinc* functions is not suitable for the interpolation of space-limited images. Therefore, several *sinc*-approximating functions: the ideal, windowed and truncated *sinc* interpolation, linear, quadratic, cubic and cubic B-spline interpolation as well as Lagrange and Gaussian methods are discussed in literature and compared the qualitative and quantitative error determinations, computational complexity evaluations, and run time measurements. The cubic B-spline interpolation has very good Fourier properties, small interpolation error and moderate computational cost. It is supposed with a regularization method it can be achieved a further advantage of B-splines over the other sinc-approximating basis functions. In image processing, when using a low-pass filter to perform image denoising, the original noisy image is firstly Fourier transformed and then the high frequency content of its spectrum is ignored. Since noise is mainly distributed over the high frequencies, all frequencies outside a circle of a prescribed radius are set to zero, and then the image is reconstructed by a 2DIFT.

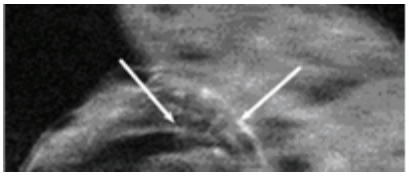

a) Keyhole method, zoom.

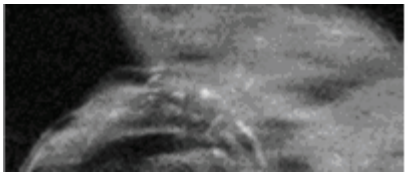

b)B-spline Keyhole method with regularization, zoom.

Fig.5. Zoomed parts of the reconstruted images.

Current method can also be used for HR of a single image, i.e in the process of obtaining a HR image given a LR one. In this simple version of the SR problem, the missing high frequency details have to be estimated in order to obtain an image with more pixels. The current B-spline model-based method called B-spline Zero-Padding (BZP) method uses B-spline basis functions to represent HR images from LR data collected in the Fourier space:

$$s(x) = \sum_{l=0}^{N_{low}-1} \alpha_l \beta_l(x), \tag{22}$$

The Keyhole-like methods were tested on real data in the *Mouse* test problem (see data sets in the site: http://mri.ifp.uiuc.edu/V/). Data consist of six data sets from a *Mouse* breast

with a big tumour: a baseline reference data set $D_B(k_x, k_y)$ and an active reference data set $D_A(k_x, k_y)$ of 256 × 256 samples, and four low-sampled data sets $D_t(k_x, k_y)$ of 32 × 256 samples, one for each dynamic section, acquired by a MR spin-echo technique after injecting a contrast agent. Figs. 5(a) and 5(b) show a zoom images by increasing the resolution of a factor 4 where it is evident that the BZP method preserves the quality of the image while the ZP method degrades the image, by introducing the artefacts indicated by the arrows.

Noniterative Interpolation-Based SR Minimizing Aliasing in the Reconstructed Image (Sanchez-Beato et al., 2008). A sampling theory framework is proposed with a pre-filtering step to allow deal with more general data models and also a specific method for SR that uses Delaunay triangulation and B-splines to build the SR image. It has been confirmed the interpolation problem solving in the case of the de-blurring with the translational motion, and with the rotations and shifts where the PSF is rotationally symmetric. The algorithm raises the following: first build a continuous function using Delaunay triangulation and then it should be projected it on the space of polynomial B splines of degree. A cubic B-spline was used, which has a good tradeoff between computational complexity and close behavior to the sampling system of *sinc* functions.

This spline $\beta^3(x)=\begin{cases} 2/3-|x|^2+|x|^3/2 & 0\le|x|<1 \\ (2-|x|)^3/6 & 1\le|x|<2 \\ 0 & 2\le|x| \end{cases}$ is employed to find the expressions needed to calculate the $a(i,j)$ coefficients.

To find the $c(i,j)$ coefficients, the impulse response of the B-spline digital filter of order seven is needed. This B-spline has Z-transform

$$S^7(z)=\frac{5040z^3}{1+120z+1191z^2+2416z^3+11191z^4+120z^5+z^6}, \tag{23}$$

which can be implemented as two recursive filters, one causal and another one anti-causal. The denominator of $S^7(z)$ has six real roots, three of them inside the unit circle and the other three outside. Separating the denominator of (23) in its causal and anti-causal parts gives: $S^7(z)=\frac{5040z^3}{1+\alpha_1 z^{-1}+\alpha_2 z^{-2}+\alpha_3 z^{-3}}\cdot\frac{1}{\gamma_1+\gamma_2 z+\gamma_3+z^3}=\frac{D(z)Y(z)}{X(z)D(z)}$, permitting to implement the *IIR* filter in such a form:

$$\begin{aligned} d(n)&=5040x(n)-\alpha_1 d(n-1)-\alpha_2 d(n-2)-\alpha_3 d(n-3) \\ y(n)&=\frac{1}{\gamma_1}\left(d(n)-\gamma_2 y(n+1)-\gamma_3(n+2)-y(n+3)\right) \end{aligned} \tag{24}$$

Initially, the first equation is run to find the $d(n)$ coefficients and then final output of the filter is obtained in the second equation. For images, this filter is applied once in the

direction x and once in the y direction. The proposed method is non-iterative, scalable and can prevent the presence of aliasing artifacts when the HR image is under-sampled suppressing the high frequency noise. Also, the Delaunay triangulation provides a very strong protection against a possible ill-conditioning of the problem. There is no parameter involved in the reconstruction that is an advantage because, in MAP methods, the gradient descent step and different parameters for the regularization prior are needed. The method is highly parallelizable, once the triangulation is done, each defined triangle independently of the others can be processed.

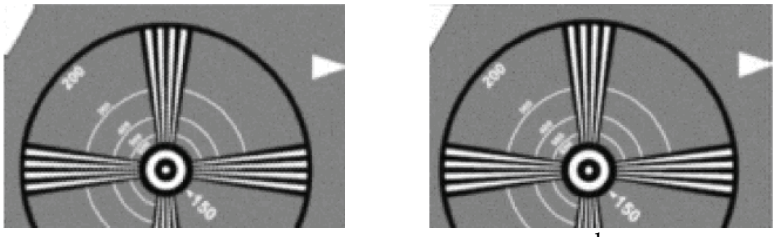

a b

Fig. 6. Super-resolved images for experiment one with SR factor 2: (a) Image with Tikhonov regularization, PSNR = 18:80dB, (b) Current method, PSNR = 19:04 dB.

The Fig.6 presents the visual results, where one can see that described method achieves the best PSNR among all tested algorithms. The borders of the lines that converge to the centre of the image present aliasing artefacts in all other methods but in current.

Estimation of the Parameters in Regularized Simultaneous SR (Zibetti et al., 2010). A method for automatic determination of the regularization parameters for the class of simultaneous SR algorithms is based on the joint maximum a posteriori (JMAP) estimation technique. This classical technique JMAP has the drawback: it can be unstable and may generate multiple local minima.

It assumes that the frame in the temporal instant k can be represented by the frame in the temporal instant j, with the motion compensated, plus a new information $e_{k,j}$, which cannot be obtained from the frame in the instant j. The motion model is defined as $\boldsymbol{f}_k = \boldsymbol{M}_{k,j}\,\boldsymbol{f}_j + \boldsymbol{e}_{k,j}$ where $\boldsymbol{f}_k$ and $\boldsymbol{f}_j$ are vectors that represent the frames in the temporal instants k and j, respectively. The matrix $\boldsymbol{M}_{k,j}$, of size $M \times M$, represents the motion transformation, or warping.

The simultaneous algorithms estimate the entire sequence of HR frames in a single process. This approach allows the inclusion of the motion matrix in the prior term, improving the quality of the estimated image sequence presenting solution as minimum of cost function:

$$\hat{f} = \arg\min_{f} \left\{ \left\| g - Df \right\|^2 + \lambda_R \left\| Rf \right\|^2 + \lambda_M \left\| Mf \right\|^2 \right\}, \tag{25}$$

where $\boldsymbol{g}$ is LR sequence, $\boldsymbol{f}$ is the HR sequence, $\boldsymbol{D}$, $\boldsymbol{R}$ are block diagonal matrixes, and $M = \begin{bmatrix} I - M_{1,2} & \cdots & 0 \\ \vdots & \ddots & \vdots \\ 0 & \cdots & I - M_{L-1,L} \end{bmatrix}$ is the first order motion difference. Because the regularization

parameters λ_M, λ_R should be known or estimated, this leads to different HR resolution algorithms.

Joint maximum a posterior (JMAP) estimation is given as a point of posterior density function:

$$\hat{f},\hat{\theta},\hat{\beta}_R,\hat{\beta}_M = \arg\max_{f,\theta,\beta_R,\beta_M} p(f,\theta,\beta_R,\beta_M / g), \tag{26}$$

where θ is data hyperparameter, and β_R, β_M are the hyperparameter of the image prior density. Using Gaussian approximations of acquisition noise, and densities $p(g/f,\theta)$, $p(f/\beta_R,\beta_M)$, it easy to find the classical JMAP estimate, according to algorithm

$$\hat{f} = \arg\min_f \ln\left(\left\|g-Df\right\|_2^2\right) + \frac{r}{LN} + \ln\left(\left\|Rf\right\|_2^2\right) + \frac{m}{LN}\ln\left(\left\|Mf\right\|_2^2\right) \tag{27}$$

Unfortunately, the cost function in is non-convex and estimation is unstable. Here, to stabilize the JMAP estimation an improved solution by modelling the JMAP hyper parameters with a Gamma prior distribution is proposed. In the JMAP method, the density of the data or the prior density of the images is connected with the density of its respective hyperparameter. For example, consider only the use of the smoothness prior, $p\left(f\middle|\beta_R\right)$, which enforces the HR images to be smooth. The associated hyperparameter β_R, defines "how smooth" is the resulting image. However, when an uniform density is assigned it is implicitly assumed that an over smooth image, like a constant intensity value image, when $\beta_R \to 0,$ is as likely to occur as a noisy image, like the one produced by a completely un-regularized estimation, when $\beta_R \to \infty,$. The other extreme choice for $p\left(\beta_R\right)$ is a Dirac delta function, i.e., an impulse in a fixed value for β_R. Among several candidates, the Gamma density has practical and theoretical advantages over the alternatives. The Gamma densities for the hyperparameters are given by $\rho\left(\theta = \frac{\theta^{(a-1)}b^{-a}}{\Gamma(a)}e^{-\frac{\theta}{b}}\right)$, and $p\left(\beta_{R,}\beta_M\right) = \frac{\beta_R^{(c-1)}\beta_m^{(h-1)}d^{-c_i-h}}{\Gamma(c)\Gamma(h)}e^{-\left[\frac{\beta_R}{d}+\frac{\beta_M}{i}\right]}$, where *a, c* and *h* are the scale factors, *b, d* and *i* are the shape factors, and $\Gamma(\mathrm{x})$ is the gamma function.

Using Gamma density functions in JMAP, the estimate it can be found as the solution:

$$\hat{f} = \arg\min_f \left(\left\|g-Df\right\|_2^2\right) + \mu_R\left(\left\|Rf\right\|_2^2\right) + \mu_M\left(\left\|Mf\right\|_2^2\right), \tag{28}$$

where parameters μ_R, μ_M depend on Gamma densities presented above.

Initial Conditions	n := 0; f_0 := initial HR image guess $\lambda_0^R =$ initial image smoothness parameter λ^R; $\lambda_0^M =$ initial motion similarity parameter λ^M; $b = D^T g$ calculate data	
initiate iterations	$A_n = D^T D + \lambda_n^R R^T R + \lambda_n^M M^T M$	MTM calculate matrix
	f_n solve via $CG\left(A_n f = b\right)$	new HR image
	$r_n^D = g - Df_n$, $r_n^R = Rf_n$	calculate data error and image smoothness
	$r_n^M = Mf_n$	calculate motion difference
	$\lambda_{n+1}^R = \mu R\left\|r_n^D\right\|2 / \left\|r_n^D\right\|2$, $\lambda_{n+1}^M = \mu M\left\|r_n^D\right\|2 / \left\|r_n^M\right\|2$	new λ^R and λ^M

Table 3. First implementation CG + parameter updating.

The first solution of the problem is presented in Table 3. The second approach (Table 4) has shown to be much faster than the first one.

Initial Conditions	$n = 0$ n := 0; $f_0 =$ HR image guess; $\lambda_0^R =$ image smoothness parameter λ^R; $\lambda_0^M =$ motion similarity parameter λ^M; $r_0 = D^T\left(Df_0 - g\right) + \lambda_0^R R^T Rf_0 + \lambda_0^M M^T Mf_0$ gradient $p_0 = -r_0$ initial search direction; $e_{0=}\left\|r_0\right\|^2$	
NL-CG iterations	$h_n = D^T Dp_n + \lambda_0^R R^T Rp_0 + \lambda_0^M M^T Mp_0$	step search A
	$\tau_n = p_n^T r_n / p_n^T h_n$	step search B
	$f_{n+1} = f_n + \tau_n p_n$	HR image update
	$r_{n+1}^D = f_n + \tau_n p_n$; $r_n^D = Df_{n+1} - g$; $r_{n+1}^M = Mf_{n+1}$	gradient part update A; gradient part update B; gradient part update C.
	$\lambda_{n+1}^R = \mu R\left\|r_{n+1}^D\right\|_2 / \left\|r_{n+1}^R\right\|_2$, $\lambda_{n+1}^M = \mu M\left\|r_{n+1}^D\right\|_2 / \left\|r_{n+1}^M\right\|_2$	new λ^R and λ^M
	$r_{n+1} = D^T r_{n+1}^D + \lambda_{n+1}^R R^T r_{n+1}^R + \lambda_{n+1}^M M^T r_{n+1}^M$	final gradient update
	$e_{n+1} = \left\|r_{n'1}\right\|^2$, $\beta_n = e_{n+1} / e_n$, $p_{n+1} = -r_{n'1} + \beta_n p_n$	search direction update
	$n = n + 1$	

Table 4. Second Implementation: NL-CG (image and parameter updated together) Present the algorithm in adequate form.

The well known *Flowers* sequence was studied in simulation experiments where the motion was estimated using the optical flow method, and in this case, linear interpolated versions of the LR images were employed. The estimated motion vectors are not completely reliable therefore, occlusions and motion errors occur in several places in the sequence.

a) b)

Fig. 7. Visual results comparing classical JMAP and the Gamma_JMAP method in two different repetitions. (a) JMAP(SNR=18.6dB; b) Gamma_JMAP (SNR=19.3dB).

In simulations, different methods in SR were probed: JMAP - The classical JMAP approach. The L-MD - The method in based in the L-Curve, designed for multiple parameters in general inverse problems. The G_JMAP-1 - Described method with the procedure, as shown in Table 3. The G_JMAP-2 - Described method with direct minimization, as shown in Table 4. Fig. 7 exposes simulation results with the tested methods. It has been noticed the instability of the JMAP and of the L-MD methods.

5. DSP Implementation

Different promising algorithms of SR realized from LR images or frames from videos have been implemented in real time mode. The heart of the EVM DM642 is a Digital Media Processor, which is based in line of C64xx Digital Signal Processors (DSPs) manufactured by Texas Instruments. DM642 is characterized by a big set of integrated peripherals inside a chip, it includes three video ports interfaces, a I2C bus controller, a multichannel serial audio port, a 64-bit EMIF, a 10/100 Ethernet Controller MAC, and a PCI interface. Characteristics card includes: A TMS320DM642 DSP at 720 MHz, 32 Mb in SDRAM, 4 Mb in Linear Memory Flash, 2 video decoders, 1 video coder, FPGA implementation to screen display, double UART with RS-232 drivers, an stereo codec, Ethernet card, 32 Kb EEPROM I2C, 8 programmable LEDs, several input-output video formats, etc. (TMS320DM642, 2004, Enry Shen, 2005). Communication of Code Composer Studio with EVM is achieved using an external emulator via JTAG connectors. Figure 8 exposes the EVM DM642 block diagram architecture. To get the processing time values, note that the TMS320DM642 DSP has a clock of 720 MHz, realizing 1.39 instructions per cycle, obtaining 570 millions instructions/sec. It is important to clarify that it can get up maximum 2,147,483,648 instructions per second.
Using Simulink module of Matlab a project is created, where the DSP model (in this case DM342EVM) and its respective Task Bios are selected; later, this bios configuration can be changed on Code Composer Studio. Inside of the function, there are three modules: video capture, subsystem realizing SR reconstruction on base of Wavelet frameworks, and video display. Next, a CCS project is formed in Simulink. The Matlab sends call to CCS, and send

the project on C. To realize the video sequence processing on DSP, first, it should be changed the MatLab program into "C" code for Code Composer Studio via Simulink. Once the project Composer Code Studio has been created, the necessary changes are arranged with purpose to obtain the processing time values. The results of time execution of the designed and reference frameworks are exposed in the next section.

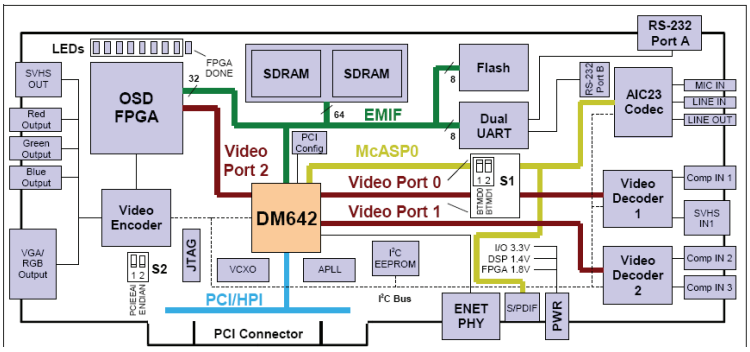

Fig. 8. Block diagram of the EVM DM642.

6. Simulation Results

Numerous statistical simulations, which have been realized, are consisted of the tests of the SR procedures in several video sequences that are widely used in the experiments: *Toy* (256x256 pixels, 8 bits), *Stephan* and *Flowers* (352 x 240 pixels, 8 bits). Additionally, the *Flowers* sequence has been reconstructed in gray scale and color formats. The first video sequence, contain an image with toys moving with defined borders, and plain background. The second one shows a tennis player, there are a lot fine details at objects like the racket, faces of the audience, etc., they are moving in several directions, moreover, the edges of the letters in the stands are exposing a visual reference. The third sequence exposes a tree with edges and field of numerous flowers that contain a lot of fine details. This sequence is used in gray and color formats. In all cases, the initial LR images are obtained reducing the original image HR size in four times, applying the summing and averaging the values of every four pixels. The reconstruction SR process should restore the initial sizes, applying different SR techniques. Finally, the original HR and reconstructed SR images are compared. The objective qualities of SR for the proposed and reference algorithms are applied according to criteria: *PSNR, MAE,* and color *NCD* measure. We also use the subjective visual comparison in form of error image to compare the capabilities of noise suppression and the artifacts´ limitations, also, the detail´s preservation of the different algorithms. There were realized numerous simulation experiments using different methods of SR reconstruction, but for each video sequence we only present below the better selected results that put in following tables (from 5 to 8) and figures (from 9 to 12). So, the reconstructed results in the SR problem for different test images using following techniques: Bi-cubic, Nearest neighbor, Warp, DCT, FFT, Sinc, Fuzzy-ELA, Recursive logic, and Wavelets based on classical families Biorthogonal, Daubechies, Symlets, Coiflets, and finally, the framework proposed show the best values in criteria PSNR and MAE for different WAF: Ξ_n, fup_n, π_n, g_n, and up_n. Finally, the

values of needed processing time for SR procedures implemented in hardware are exposed for better algorithms.
In the SR frame of the video sequence *Toy*, one can observe the simulation results in Table 5 and Fig.9 comparing the original HR and LR images that the better performance in terms of objective criteria PSNR and MAE, as well as in subjective perception are presented employing SR reconstruction on the base of WAF fup_1 and DCT algorithm. It is clearly observed in the images (see Fig.9) better subjective perception for WAF fup_1 in comparison with DCT technique.

		Algorithm	MAE	PSNR	Algorithm	MAE	PSNR
No. of frame	1	fup_3	*12.36*	*34.76*	**DCT**	*12.09*	*34.90*
	2		*12.67*	*34.65*		*12.45*	*34.59*
	3		*12.78*	*34.56*		*12.43*	*34.61*
	1	fup_1	**11.38**	**34.91**	**Daubechies**	13.20	34.50
	2		**11.35**	**34.90**		13.44	34.37
	3		**11.51**	**34.90**		13.55	34.34

Table. 5. Objective criteria values for video sequence *Toy*.

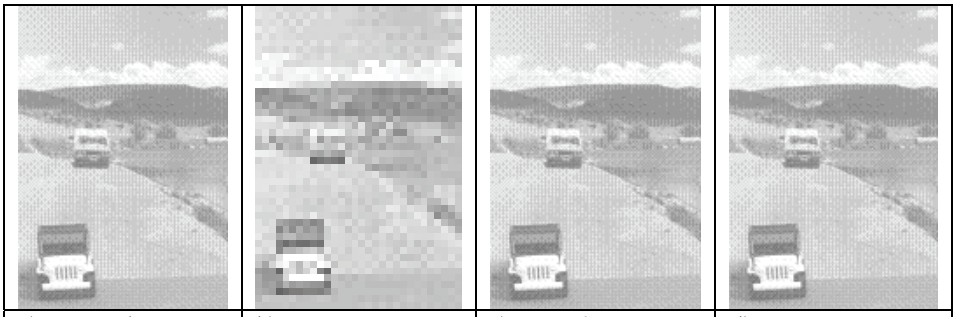

a) Original HR. b) Input LR. c) WAF fup_1. d) DCT.

Fig. 9. Visual perception results for the video sequence *Toy*.

Video sequence *Stephan* has several features, one of which is that there are several movements in it as above mentioned. The simulation results expose the best reconstruction in SR process in the case of WFA usage. This is confirmed as in objective criteria for fine details (see Table 6, MAE), as in subjective perception analyzing SR reconstructed images and corresponding error images (Fig.10).
In the video sequence *Flowers* (see Table 7 and Fig.11), there is clear the difference between LR image and HR one, because of numerous fine features presented in the flowers. Also, there are the well-defined borders of the house. Better results among all analyzed algorithms in terms of the objective criteria are presented by DCT algorithm and when the WAF π_6 is employed, but observing the SR images and their error images it can viewing that mentioned WAF exposes in some areas slightly better visual subjective performance.

No. of Frame		Algorithm	MAE	PSNR	Algorithm	MAE	PSNR
	100		**5.10**	**80.10**		*6.59*	*80.43*
	200		**3.01**	**82.29**		*3.98*	*83.44*
	300	π_5	**2.61**	**83.05**	biorthogonal	*4.81*	*82.23*
	100		***5.90***	***79.44***		51.73	72.38
	200		***3.18***	***82.01***		23.68	73.47
	300	Ξ_3	***2.88***	***82.48***	Coiflets	29.90	72.77

Table. 6. Objective criteria values for video sequence *Stephan*.

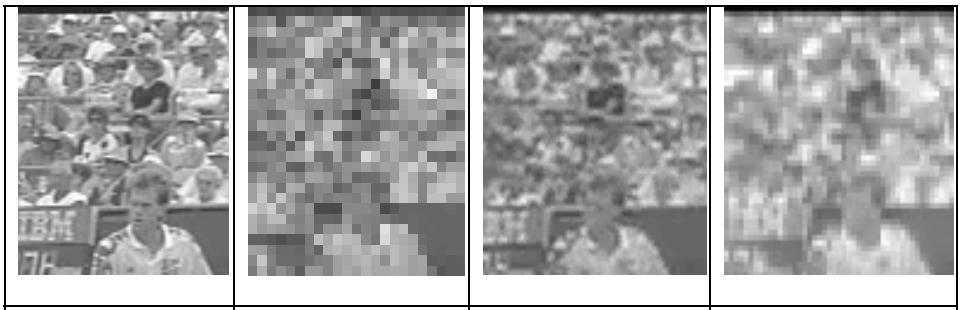

a) Original HR. b) Input LR. c) WAF π_5. d) Biorthogonal.

Fig. 10. Visual perception results for the video sequence *Stephan*.

The main difference of the color video sequence *Flowers* (Fig.12) in comparison with their gray variant (Fig.11) is additional color information that permits to see more precisely the fine details for flowers in different colors. For example, analyzing SR image restored employing the WAF π_5 or Ξ_3, one can see better visual performance in comparison with any another SR restoration algorithm. For example, SR procedure based on Biorthogonal Wavelet presents blurry frames with the pixels having a sideways movement type, moreover, the values in the error images are greater for the SR algorithm in case Biorthogonal than when the SR based on the WAF π_5 and Ξ_3 are employed.

No. Of frames		Algorithm	MAE	PSNR	Algorithm	MAE	PSNR
	10		11.40	76.88		**9.57**	**78.27**
	15		9.11	78.18		**8.65**	**78.55**
	20	π_5	9.97	77.31	DCT	**8.05**	**78.66**
	10		*9.97*	*77.31*		63.08	72.53
	15		*9.11*	*78.18*		54.22	72.60
	20	π_6	*11.40*	*76.88*	Coiflets	59.97	72.51

Table. 7. Objective criteria values for video sequence *Flowers* (gray).

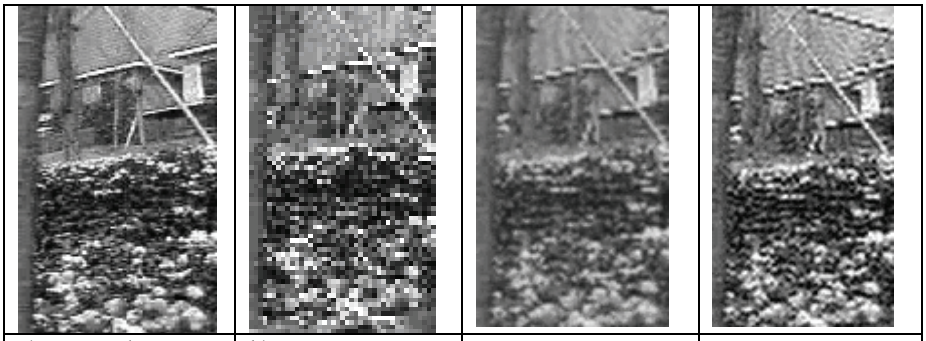

a) Original HR. b) Input LR. c) WAF π_5. d) DCT.

Fig. 11. Visual perception results for the video sequence *Flowers*.

No. of Frame		Algorithm	MAE	PSNR	NCD	Algorithm	MAE	PSNR	NCD
	10		**11.00**	**79.17**	**0.09**		***11.08***	***76.74***	***0.197***
	15		**10.24**	**79.43**	**0.09**		***12.12***	***76.24***	***0.205***
	20	**Biorthogonal**	**9.88**	**79.49**	**0.08**	Ξ_3	***10.52***	***76.73***	***0.182***

Table. 8. Objective criteria values for video sequence *Flowers* (colour).

Finally, the results of real time implementation are presented for the SR algorithms on DSP. Table 9 exposes the values of processing time for different better SR algorithms tested here. The first and second columns mark the class and type of algorithm, in the third and fourth columns, the results obtained in Matlab implementation are presented; the fifth and sixth columns show the DSP processing time values, and, finally the seventh and eighth columns view the processing results on DSP serial processing.

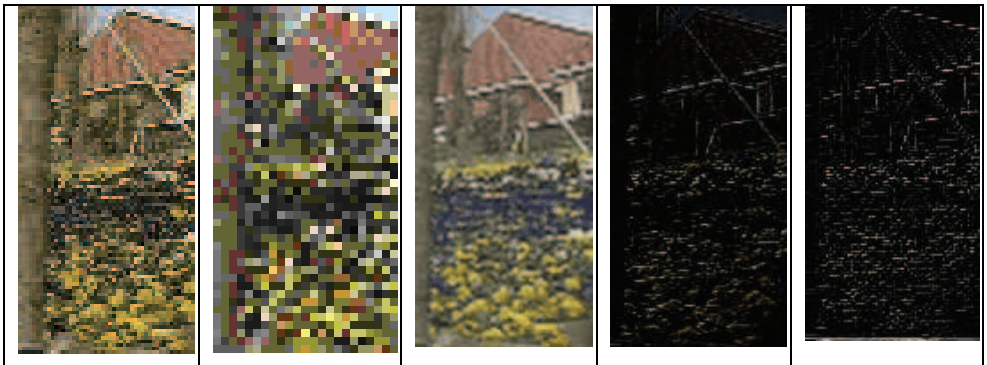

a) Original HR. b) Input LR. c) WAF Ξ_3. d) WAF Ξ_3. Error image. Biorth. Error image.

Fig. 12. Visual results for the *Flowers* (colour) sequence.

One can observe that dividing the WAF configuration process into two parts, the serial processing on DSP reduces the processing time values, presenting the better processing

performance, resulting in 25.43 frames per second for WAF technique. This can be considered as practically on line real-time processing.

Processing Time Values, sec				Processing Time Values, sec			
Time in seconds		*Matlab*		*DSP*		*Serial Processing on DSP*	
Type	*Algorithm*	*Time/ frame*	*Frame/ sec*	*Time/ frame*	*Frames/s*	*Time/frame*	*Frames/ s*
Others	***Bicubic***	*0.03*	*33.33*	*0.07074*	*14.1363*	*0.03338*	*29.958*
	Nearest neighbour	*0.03*	*33.33*	*0.07074*	*14.1363*	*0.03358*	*29.780*
	Bilineal	*0.03*	*33.33*	*0.07074*	*14.1363*	*0.03338*	*29-958*
	DCT	*0.084*	*11.90*	*0.20028*	*4.9930*	*0.03343*	*29.913*
Wavelets	***Biorth.***	*0.075*	*13.33*	*0.17685*	*5.6545*	*0.02989*	*33.456*
	Coiflets	*0.075*	*13.33*	*0.17685*	*5.6545*	*0.02989*	*33.456*
	Daubechies	*0.075*	*13.33*	*0.17685*	*5.6545*	*0.02989*	*33.456*
	Symlets	*0.075*	*13.33*	*0.17685*	*5.6545*	*0.02989*	*33.456*
WAF	$\Xi_i(x)$, $i=\overline{2,4}$	*0.04*	*25.00*	*0.09432*	*10.6022*	*0.03932*	*25.432*
	$fup_i, i=1,4;8$	*0.04*	*25.00*	*0.09432*	*10.6022*	*0.03932*	*25.432*
	$g_i, \quad i=\overline{2,6}$	*0.04*	*25.00*	*0.09432*	*10.6022*	*0.03932*	*25.432*
	$\pi_i, \quad i=\overline{2,6}$	*0.04*	*25.00*	*0.09432*	*10.6022*	*0.03932*	*25.432*
	$up_i, \quad i=\overline{2,4,7,8}$	*0.04*	*25.00*	*0.09432*	*10.6022*	*0.03932*	*25.432*

Table 9. Values of processing time in hardware implementation.

7. Conclusion

It has realized a review of several promising SR methods. Some of them are usually focused on solving the issue of super resolution only for some specific type of image, or images that are used in specific applications, others, need to have additional prior information about the image, perform some sort of convergence of information, or realize some training, this, before processing the information and get the SR image. The proposed method can be applied to any kind of image or video sequence frame without any a priory information, permitting to realize the SR process over the region of interest of an image, a sequence of images and video, it is not depended on the type of application where it was obtained, and it much less interfere with results from the final purpose image. Additionally, numerous simulation and real time implementation results have shown that the proposed framework based on the WAFs is effective in performing the image registration and super-resolution for different real-life video sequences, demonstrating better robust performance in the frames with different nature and texture characteristics, such as edges, fine details, and different types of movements. Real time implementation of the proposed framework on

MatLab and DSP platforms has confirmed the processing velocity of about 25 frames/sec for all investigated video sequences.

Acknowledgement

The authors thank the National Polytechnic Institute of Mexico and CONACYT (grant 81599) for their support to realize this work.

8. References

Akgun T., Altunbasak Y., Mersereau R. M. (2005). Super-resolution reconstruction of hyperspectral images, *IEEE Trans. on Image Proc.* Vol.14, No.11, 2005, pp.1860–1875, ISSN: 1057-7149.

Baboulaz L. and Dragotti P. L. (2009). Exact feature extraction using finite rate of innovation principles with an application to image super-resolution. *IEEE Trans. on Image Proc.*, vol. 18, No. 2, 2009, pp. 281–298, ISSN: 1057-7149.

Bovik A.,Ed.(2000).*Handbook of Image and Video Process*.Academic.ISBN:0-12-119790-5, MA.

Callico G.M., Lopez S., Sosa O., Lopez J.F., and Sarmiento R. (2008). Analysis of fast block matching motion estimation algorithms for video super-resolution systems. *IEEE Trans. on Consumer Elec.*, Vol.54, No. 3, 2008, pp.*1430-1438,* ISSN*:* 0098-3063*.*

Chan R., Chan T., Shen L., Shen Z. (2003). Wavelet algorithms for high-resolution image reconstruction, *SIAM Journal on Scientific Computing*, Vol. 24, No.4, 2003, 1408–1432, ISSN: 1064-8275.

Chaudhuri S. (2001). *Super-Resolution Imaging*, Kluwer Academic Publ., ISBN: 0-7923-7471-1. MA, USA.

Chaudhuri S. and Manjunath J. (2005). *Motion-Free Super-Resolution*. Springer, ISBN-13: 978-0387-25587-3.New York.

Crouse M. S., Nowak R. D., and Baranuik R. G. (1998). Wavelet based signal processing using hidden Markov models, *IEEE Trans. on Signal Proc.* Vol.46, No. 4, 1998, pp. 886-902. ISSN: 1053-587X.

Enry Shen. Code Compouser Studio (optimization), Texas Instruments (2005), *Proc. Of 8th Texas Instruments Developer Conference,* India, Bangalore, 2005.

Farsiu S., Robinson D., Elad M., and Milanfar P. (2004).Advances and chanllenges in super-resolution,"*Int.J.Imaging Syst. Techn.* Vol.14, No.2, 2004, pp.47–57, ISSN: 0899-9457.

Farsiu S., Elad M., and Milanfar P. (2006). Video-to-video dynamic superresolution for grayscale and color sequences. *EURASIP J. Appl. Signal Process*. Vol.10, 61859_1-10, 2006, ISSN: 1110-8657.

Flusser F., Sroubek, J. (2003). Multichannel blind iterative imagerestoration. *IEEE Trans. Image Process*. Vol.12, No.9, 2003, pp.1094–1106, ISSN:1110-8657.

Franzen O., Tuschen C., Schroeder H.(2001).Intermediate image interpolation using polyphase weighted median filters, *Proc. SPIE*, vol. 4304, pp.306–317, ISSN 0277-786X. 2001.

Gomeztagle F., Kravchenko V., and Ponomaryov V. (2009). Super-Resolution Procedures in Images and Video sequences Applying Wavelet Atomic Functions" in *Proc. of IASTED 20th Symposium on Modelling and Simulations*, pp.187-189, ISBN: 978-0-88986-798-7. Banff, Alberta, Canada, 2009.

Gulyaev Yu.V., Kravchenko V.F., Pustovoit V.I. (2007). A New Class of WA-Systems of Kravchenko–Rvachev Functions, *Doklady Mathematics*, Vol.75, No.2, 2007, pp.325–332, ISSN:1064-5624.

Hou H. S. and Andrews H. C. (1978).Cubic splines for image interpolation and digital filtering, *IEEE Trans. on Accoust., Speech and Sig. Proc.*, Vol.26, No.6, 1978, 508– 517, ISSN:0096-3518.

Jain J.R. and Jain A.K. (1981). Displacement measurement and its application in interframe image coding. *IEEE Trans. On Commun.*, Vol. 29, No. 12, 1981, pp. 1799-1808, ISSN: 0090-6778.

Juarez C., Ponomaryov V., and Kravchenko V.F. (2008). Wavelets Based on Atomic Function used in Detection and Classification of Masses in Mammography, *Lect. Not. in Art. Intel.*, LNAI 5317, 2008, pp.295-304, ISSN:0302-9743.

Katsaggelos A., Molina R., and Mateos J. (2007). *Super Resolution of Images and Video, Synthesis Lectures on Image, Video, and Multimedia Processing*. Morgan & Claypool, ISBN:1-5982-90843. New York.

Kravchenko V.F., Ponomaryov V.I., Sanchez-Ramirez J.L. (2008). Properties of Different Wavelet Filters used for Ultrasound and Mammography Compression, *Telecom. and Radio Engineering.*, Vol.87, No.10, 2008, pp.853-865, ISSN:0040-2508.

Kravchenko Victor, Perez-Meana Hector, and V .Ponomaryov. (2009). *Adaptive Digital Processing of Multidimensional Signals with Applications*, FizMatLit Edit., ISBN:978-5-9221-110-6. Moscow (available in http://www.posgrados.esimecu.ipn.mx).

Landi G. and Loli Poicolomimi E. (2006). Representation of High Resolution Images from Low Sampled Fourier Data: Applications to Dynamic MRI. *J Math Imaging Vision*, 2006, pp. 27–40, ISSN:0924-9907.

Lertrattanapanich S., Bose N. K. (2002). High resolution image formation from low resolution frames using Delaunay triangulation, *IEEE Trans. on Image Proc.,* Vol. 11, No.12, 2002, pp. 1427–1441, ISSN: 1057-7149.

Luisier F., Blu T., and Unser M. (2007). A new sure approach to image denoising: Inter-scale orthonormal wavelet thresholding. *IEEE Trans. on Image Proc.,* V. 16, No. 3, 2007, pp. 593–606, ISSN: 1057-7149.

Ng M. K., Sze C. K., Yung S. P. (2004). Wavelet algorithms for deblurring models. *Intern. Jour. of Imaging Systems and Techn*. V. 14, No.3, 2004, pp.113–121, ISSN 0010-4620 .

Maeland E. (1998). On the comparison of interpolation methods, *IEEE Trans. on Med. Imag.* Vol.7, No.3, 1998, pp.213–217, ISSN: 0278-0062.

Meyer Y.(1990). *Ondelettes,* Hermann, Paris, France (in French), ISBN: 0-8218-13870.

Park S., Park M., and Kang M. (2003). Super-resolution image reconstruction: A technical overview. *IEEE Sign. Proc. Mag.*, vol. 20, No. 3, 2003, pp. 21–36, ISSN: 1053-5888.

Phu M.Q., Tischer P.E., Wu H.R. (2004). A median based interpolation algorithm for deinterlacing, *Proc. of Int. Symp.on Intellig. Sign. Proc. and Commun. Systems,* pp.390–397, ISBN: 0-7803-8639-6. Seoul. 2004.

Protter M., Elad M., Takeda H., and Milanfar P. (2009). Generalizing the non-local-means to super-resolution reconstruction. *IEEE Trans on Image Proc.*, vol. 16, No. 2, 2009, pp. 36–51, ISSN: 1057-7149.

Reichenbach S.E.. Geng F. (2003). Two-dimensional cubic convolution. *IEEE Trans on Image Proc*. Vol.12, No.8, 2003, pp.857–865, ISSN :1057-7149.

Qin Feng-qing, He Xiao-hai, Chen Wei-long, Yang Xiao-min, Wu Wei. (2009). Video superresolution reconstruction based on subpixel registration and iterative back projection. *J. of Elect. Imaging,* Vol.18, No.1, 2009, 013007_1-11, ISSN: 1017-9909.

Sanchez-Beato A. and Pajares G. (2008). Noniterative Interpolation-Based Super-Resolution Minimizing Aliasing in the Reconstructed Image. *IEEE Trans. On Image Proc.*, Vol.17, No. 10, 2008, p.1817-1826, ISSN : 1057-7149.

Shen Huanfeng, Zhang Liangpei, Huang Bo, and Li Pingxiang. (2007). A MAP Approach for Joint Motion Estimation, Segmentation, and Super Resolution. *IEEE Trans. On Image Proc.*, V.16, No. 2, 2007, pp. 479-490, ISSN : 1057-7149.

Sroubek F., Flusser J. (2006). Resolution enhancement via probabilistic deconvolution of multiple degraded images,Institute of Information Theory and Automation, *Pattern Recognition Letters,* Vol. 27, No.4 , 2006, pp.297-283, ISSN: 0167-8655.

TMS320DM642 Evaluation Module with TVP Video Decoders (2004). *Technical Reference* 507345-0001 Rev. B, December 2004.

Tolpekin V.A and Hamm N.A.S. (2008). Fuzzy super-resolution mapping based on Markov random fields. *Proc. Of IEEE Int. Geosc. & Remote Sensing Symp.* pp.96-99, ISBN: 978-1-4244-2807-6. 2008.

Wang C. and Xue P. (2006). Improved super-resolution reconstruction from video. *IEEE Trans.Circuits Syst. Video Technol.* Vol.16, No.11, 2006, pp.1411–1422,ISSN:1051-8215.

Wood S.L., Lee S.-T., Yang G., Christensen M.P., Rajan D. (2008). Impact of measurement precision and noise on superresolution image reconstruction, *Appl. Opt*., Vol. 47, No.10, 2008, pp.1638–1648, ISSN: 0003-6935.

Wood Sally L. (2009). Super-resolution image reconstruction for a steerable array of sub-imagers. *Digital Signal Processing.* Vol. 19, , No.6, 2009, pp. 923–933, ISSN:1051-2004.

Wüst Zibetti M. V., and Mayer Joceli A. (2007). Robust and Computationally Efficient Simultaneous Super-Resolution Scheme for Image Sequences. *IEEE Trans. On Circ. And System for Video Tech.*, Vol. 17, No. 10, 2007, pp.1288-1300, ISSN: 1051-8215.

Zhang Liangpei, Zhang Hongyan, Shen Huanfeng, Li Pingxiang. (2010). A super-resolution reconstruction algorithm for surveillance images. *Signal Processing*. 2010. doi: doi:10.1016/j.sigpro.2009.09.002, Ref.: SIGPRO3898, ISSN:0165-1684.

Zibetti W., M.V., Bazan V. F.S., Mayer, J. (2010). Estimation of the Parameters in Regularized Simultaneous Super-resolution, *Pattern Recognition Letters*. 2009, doi: 10.1016/j.patrec.2009.12.009. ISSN: 0167-8655.

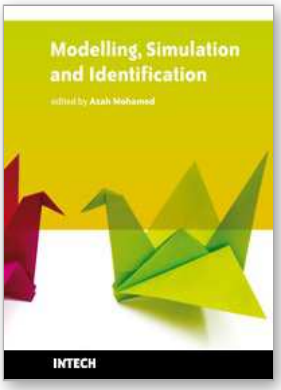

Modelling, Simulation and Identification

Edited by Azah Mohamed

ISBN 978-953-307-136-7
Hard cover, 354 pages
Publisher Sciyo
Published online 18, August, 2010
Published in print edition August, 2010

Modeling, simulation and identification has been actively researched in solving practical engineering problems. This book presents the wide applications of modeling, simulation and identification in the fields of electrical engineering, mechanical engineering, civil engineering, computer science and information technology. The book consists of 17 chapters arranged in an order reflecting multidimensionality of applications related to power system, wireless communication, image and video processing, control systems, robotics, soil mechanics, road engineering, mechanical structures and workforce capacity planning. New techniques in signal processing, adaptive control, non-linear system identification, multi-agent simulation, eigenvalue analysis, risk assessment, modeling of dynamic systems, finite difference time domain modeling and visual feedback are also presented. We hope that readers will find the book useful and inspiring by examining the recent developments in the applications of modeling, simulation and identification.

How to reference

In order to correctly reference this scholarly work, feel free to copy and paste the following:

Volodymyr Ponomaryov and Francisco Gomeztagle (2010). Super-Resplution Procedures in Images and Video Sequences Based on Wavelet Atomic Functions, Modelling, Simulation and Identification, Azah Mohamed (Ed.), ISBN: 978-953-307-136-7, InTech, Available from: http://www.intechopen.com/books/modelling--simulation-and-identification/super-resolution-procedures-in-images-and-video-sequences-based-on-wavelet-atomic-functions

INTECH
open science | open minds

InTech Europe
University Campus STeP Ri
Slavka Krautzeka 83/A
51000 Rijeka, Croatia
Phone: +385 (51) 770 447
Fax: +385 (51) 686 166
www.intechopen.com

InTech China
Unit 405, Office Block, Hotel Equatorial Shanghai
No.65, Yan An Road (West), Shanghai, 200040, China
中国上海市延安西路65号上海国际贵都大饭店办公楼405单元
Phone: +86-21-62489820
Fax: +86-21-62489821